

Article

Combination of High-Resolution Optical Coherence Tomography and Raman Spectroscopy for Improved Staging and Grading in Bladder Cancer

Daniela Bovenkamp ^{1,†}, Ryan Sentosa ^{1,†}, Elisabet Rank ¹, Mikael T. Erkkilä ¹, Fabian Placzek ¹, Jeremias Püls ¹, Wolfgang Drexler ¹, Rainer A. Leitgeb ¹, Nathalie Garstka ², Shahrokh F. Shariat ², Clara Stiebing ³, Iwan W. Schie ³, Jürgen Popp ³, Marco Andreana ^{1,*} and Angelika Unterhuber ¹

¹ Center for Medical Physics and Biomedical Engineering, Medical University of Vienna, Waehringerguertel 18-20, 1090 Vienna, Austria; daniela.bovenkamp@meduniwien.ac.at (D.B.); ryan.sentosa@meduniwien.ac.at (R.S.); elisabet.rank@meduniwien.ac.at (E.R.); mikael.erkkilae@meduniwien.ac.at (M.T.E.); fabian.placzek@meduniwien.ac.at (F.P.); jeremias.puels@meduniwien.ac.at (J.P.); wolfgang.drexler@meduniwien.ac.at (W.D.); rainer.leitgeb@meduniwien.ac.at (R.A.L.); angelika.unterhuber@meduniwien.ac.at (A.U.)

² Department of Urology, Medical University of Vienna, Waehringerguertel 18-20, 1090 Vienna, Austria; nathalie.garstka@meduniwien.ac.at (N.G.); shahrokh.shariat@meduniwien.ac.at (S.F.S.)

³ Leibniz Institute of Photonic Technology, Albert-Einstein-Str. 9, 07745 Jena, Germany; clara.stiebing@leibniz-ipht.de (C.S.); iwan.schie@leibniz-ipht.de (I.W.S.); juergen.popp@ipht-jena.de (J.P.)

* Correspondence: marco.andreana@meduniwien.ac.at

† Both authors contributed equally to this work

Received: 15 October 2018; Accepted: 20 November 2018; Published: 23 November 2018



Featured Application: Optical coherence tomography (OCT) and Raman spectroscopy (RS) evaluated with Principal Component Analysis (PCA) and k-nearest neighbor classification (kNN).

Abstract: We present a combination of optical coherence tomography (OCT) and Raman spectroscopy (RS) for improved diagnosis and discrimination of different stages and grades of bladder cancer *ex vivo* by linking the complementary information provided by these two techniques. Bladder samples were obtained from biopsies dissected via transurethral resection of the bladder tumor (TURBT). As OCT provides structural information rapidly, it was used as a red-flag technology to scan the bladder wall for suspicious lesions with the ability to discriminate malignant tissue from healthy urothelium. Upon identification of degenerated tissue via OCT, RS was implemented to determine the molecular characteristics via point measurements at suspicious sites. Combining the complementary information of both modalities allows not only for staging, but also for differentiation of low-grade and high-grade cancer based on a multivariate statistical analysis. OCT was able to clearly differentiate between healthy and malignant tissue by tomogram inspection and achieved an accuracy of 71% in the staging of the tumor, from pTa to pT2, through texture analysis followed by k-nearest neighbor classification. RS yielded an accuracy of 93% in discriminating low-grade from high-grade lesions via principal component analysis followed by k-nearest neighbor classification. In this study, we show the potential of a multi-modal approach with OCT for fast pre-screening and staging of cancerous lesions followed by RS for enhanced discrimination of low-grade and high-grade bladder cancer in a non-destructive, label-free and non-invasive way.

Keywords: optical coherence tomography (OCT); Raman spectroscopy (RS); principal component analysis (PCA); k-nearest neighbor classification (kNN); bladder cancer

1. Introduction

Cancer is one of the leading causes of mortality worldwide [1–3]. Bladder cancer has not only the highest recurrence rate amongst all cancer types, but also ranks as thirteenth in the context of mortality [4,5]. Hence, early diagnostic and full resection of suspicious lesions need to be improved to minimize the likelihood of recurrence. Currently, the gold standard for bladder cancer detection is white light-guided cystoscopy (WLC) with transurethral resection of the bladder tumor (TURBT). The resected bladder biopsies are examined by histopathologists. As this method heavily depends on the subjective interpretation of the surgeon and the histopathologist, it is time-consuming and associated with high costs, therefore new strategies to overcome these limitations are of interest. Furthermore, the main disadvantage of conventional WLC is its lack of sensitivity to detect small lesions as stage Ta/T1 tumor or carcinoma in situ. Ta describes the stage of a tumor, which is superficial and does not invade the subepithelial connective tissue. T1 indicates the stage of tumor infiltrating the subepithelial connective tissue. T2 tumor invades the muscle and stage T3 tumor further penetrates perivesical tissue. T4 tumor reaches prostate stroma, seminal vesicles, uterus, vagina, pelvic wall or abdominal wall (TNM classification 2009). Several approaches, e.g., ultrasound, photodynamic diagnosis, narrow-band imaging, confocal laser endo-microscopy to improve diagnostics and potentially diagnose in vivo have been proposed [6–8].

Optical coherence tomography (OCT) is a label-free optical technique based on low coherence light interferometry allowing for fast cross-sectional views of tissue structure [9–11]. As this method is non-invasive, non-destructive and label-free it has found broad application in diagnostic of different types of skin cancer, oral cancer, lung cancer, breast cancer, colon cancer, prostate cancer and esophageal cancer [12]. Yuan et al. showed a combined OCT and ultrasound approach to investigate bladder cancer in a rat model [13]. In this study, diagnosis of bladder diseases were performed on inflammatory tissue and different stages of the tumor (Ta, T1, T2, T3 and T4). In previous studies, OCT has lacked discrimination of the different stages, due to limited imaging depth as further degenerated tumors infiltrated the muscle too deep. This limitation could be overcome by switching to longer interrogation wavelengths. Despite this drawback, OCT for human bladder cancer detection revealed clearly different structural features of healthy bladder tissue compared to carcinoma in situ and furthermore different stages of bladder cancer [14,15]. As OCT imaging is limited to extract morphological features, no diagnosis of grading can be achieved. However, extraction of texture features in OCT images allows for automated analysis and is capable of discriminating healthy and pathologic tissue. First approaches to texture analysis were demonstrated on mouse lung tissue [16]. Furthermore, the feasibility of such an algorithm has been shown on the diagnosis of breast tissue [17]. As these algorithms look for textural features of OCT images, this approach can also be applied to OCT images acquired in the bladder discriminating different stages. Even though the lack to provide molecular information restricts OCT to the staging of bladder tissue via morphological features, grading still needs to be complemented by another modality.

Raman spectroscopy (RS) is based on the inelastic light scattering between a photon and a molecule and the thereby excitation of molecular vibrations, providing molecular fingerprint information of the sample. The method has been widely used to successfully achieve discrimination between cancerous versus healthy tissue [18–24]. Complementary to OCT, RS provides high chemical sensitivity and can detect the smallest molecular changes between healthy and diseased tissue. First RS investigations on bladder examined the bladder wall layers [25], followed by approaches to differentiate between tumor and non-tumor bladder tissue [26,27]. Analysis of the biochemistry in bladder lesions was explored by Stone et al. to understand the molecular changes associated with different bladder cancer grades [28]. Draga et al. demonstrated the feasibility of RS for in vivo bladder cancer detection with an endoscope [29]. Recently, the feasibility of low-resolution RS for biological samples was introduced for the first time by Schie et al. [30] and implemented by Chen et al. in a fiber-optic probe for the diagnosis of bladder cancer [31], strengthening the potential of RS as a diagnostic tool in bladder cancer.

The combination of OCT with spontaneous RS provides complementary information on the structural changes and the associated molecular differences in tissue. While OCT provides high speed 3D structural information from large areas and can be used as a red-flag technology, RS can identify the full molecular fingerprint of tissue. The qualitative and quantitative molecular information obtained with RS can be localized with high-speed high-resolution OCT revealing structural information with μm isotropic resolution. First OCT-RS combinations have been tested in colon [32], retina [33], atherosclerotic plaques, [34] and skin [35,36].

We report on a multi-modal OCT and RS approach to explore its capabilities to increase the accuracy of the staging and grading of suspicious lesions in the bladder wall *ex vivo* by the combination of these complementary techniques.

2. Materials and Methods

This study and its procedures are approved by the ethics committee of the medical university of Vienna (code: 1577/2017).

2.1. Patients

12 Bladder biopsies originating from eight patients (one woman, seven men) were included in this study. Bladder biopsies were resected via TURBT and measured not later than 30 min after surgery. Histopathology was performed on all samples. Distribution of histology among patients comprised five pTa, two pT1 and one pT2 staged and four low-grade and four high-grade urothelial carcinomas. As OCT data were collected per patient and RS data per biopsy, the distribution of histology among the biopsies was as followed: Seven low-grade and five high-grade tumors. Tissue samples were carefully placed onto quartz microscope slides, with the urothelium being oriented upwards, to ensure minimum interference of the Raman signals from bladder tissue with the autofluorescence from the microscope slides (Alfa Aesar, Thermofisher, Waltham, MA, USA). As illustrated in Figure 1, OCT measurements were performed to identify suspicious lesions via visual inspection to discriminate healthy bladder wall from the pathologic tissue, as described by Schmidbauer et al. [15] and to determine its position and depth. The suspicious regions of interest (ROI) identified by OCT were then measured by RS.

2.2. OCT System

The spectral domain optical coherence tomography (SDOCT) system was built into a customized upright laser scanning microscope (Eclipse E400, Nikon, Tokyo, Japan) equipped with a $10\times$ air objective ($10\times$, NA 0.25, Nikon CFI Achrom). Light source for the OCT system was a broadband Ti:Sapphire laser (800 nm central wavelength, 150 nm bandwidth at full width half maximum) and 75 MHz repetition rate. The maximum power on the sample was 2.5 mW. Galvanometric mirrors were implemented for scanning the sample plane (6220H, Cambridge Technology, Bedford, MA, USA). OCT signal detection was achieved with a spectrometer consisting of 1200 lines per mm grating (Wasatch Photonics, Logan, UT, USA) and 840 nm central wavelength and 12bit CCD-based line scan camera with a maximum line rate of 70 kHz and 2048 pixels (AViiVA Atmel EM4CL 2014, Essex, UK). The signal-to-noise ratio was determined to be 97 dB. The SDOCT system had an axial resolution of $1.5\ \mu\text{m}$ and lateral of $2.2\ \mu\text{m}$, respectively. The field of view (FOV) for all the measurements was $\sim 1.2 \times 1.2\ \text{mm}$ and the depth range covers 1.3 mm. Collection of OCT data were controlled via an in-house written Matlab software. The live view OCT operated at 20 B-scans per second, including real-time processing allowing for navigation and screening without noticeable time lag. The acquisition time for an OCT volume was 66 s. Each raw OCT data consists of $2048 \times 800 \times 4000$ voxels, which includes five times repetition at every B-Scan position. After performing Fourier transformation and five times averaging, the processed OCT data set ($1024 \times 800 \times 800$ voxels) were further analyzed, as described in Section 2.4 and illustrated in Figure 1.

2.3. RS System

The RS system comprised of a 785 nm diode laser (VBG-Stabilized Single Laser Source, LS-1-78-1-FA), which was focused onto the sample of interest by a microscope objective (20×, NA 0.4, Newport), and a spectrometer (Shamrock SR 303i, Andor Technology, Belfast, Northern Ireland) equipped with a CCD-camera with 255 × 1024 pixels (Newton 920i, Andor Technology) to record the Raman signal. The laser has a maximum output power of 600 mW and was free-space coupled to the system. To remove unwanted side-lobes, a laser clean-up filter (LL01-785-12.5, Semrock 785 nm MaxLine®) was integrated. For the excitation of the Raman signal, 100 mW was delivered to the sample plane. The microscope objective achieved a spot size of 10 μm and a Rayleigh length of 36 μm. The spectrometer was equipped with a 300 L/mm grating blazed at 500 nm, and the slit size was set to 50 μm. Raman spectra were collected in a range from 300–3200 cm⁻¹ with a resolution of approximately 0.5 nm corresponding to a spectral resolution varying from 7 cm⁻¹ at 300 cm⁻¹ to 4 cm⁻¹ at 3200 cm⁻¹. The RS system was designed for epi-detection to mimic the detection geometry using an endoscope. To separate the Raman signal from the laser light, a short pass dichroic mirror with a cut-off wavelength of 805 nm (DMSP805, Thorlabs, Newton, NJ, USA) was used. To remove residual photons from the laser excitation an ultra-steep long-pass edge filter (LP02-785RE-25, Semrock 785 nm RazorEdge®) was used. The RS setup was wavelength-calibrated using Dimethylsulfoxid (DMSO) and paracetamol [37–39]. Bladder biopsies were placed on quartz microscope slides as quartz does not exhibit Raman signals compared to soda lime glass. On average 20 Raman spectra were collected from each bladder specimen with an integration time of 10 s and a three-fold accumulation. Acquisition of Raman spectra was performed, using the commercial software Andor Solis.

2.4. OCT Texture Analysis

We performed texture analysis to extract features from OCT images using Matlab. Figure 1 illustrates the process of data analysis. Previous studies developed texture analysis algorithms that extracted different features from OCT images [16,17]. For every acquired B-Scan of the OCT volumes, the gray-level co-occurrence matrix was computed and four statistical values, namely: Contrast, correlation, energy, and homogeneity, were obtained. This was repeated to determine the values for the interrogation angles 0, 45, 90, 135 degrees, which determines the orientation of the texture relative to the horizontal line. Note that no preprocessing or cropping of the OCT volume was performed prior to this analysis. Thus, 16 features were generated per B-Scan. After processing the whole volume, the number of features was reduced to avoid single, corrupted B-Scans to falsify the classification. Therefore, the volume was divided by B-Scans into 10 parts and the mean, median, maximum, minimum, and standard deviation of the features were computed within the batch. This resulted in overall five times 16 features per batch, which generated in total a feature vector with 80 observations (8 OCT volumes) and 80 features. One OCT dataset per patient was evaluated. Prior to classification the feature vector was normalized to [0,1] to assure the correct interpretation of the principal component analysis (PCA) and k-nearest neighbor (kNN) classifier. The processing of the OCT volume from the acquired spectra, as well as the texture analysis took approximately 10 min.

2.5. RS Analysis

Raw Raman spectra were corrected for wavelength dependent transmission losses of the optical elements and quantum efficiency of the detector using the system transfer function as depicted in Figure 1. The fluorescent background was removed using an iterative polynomial fitting algorithm (polynomial order 9) [40] and smoothed using Savitzky-Golay filtering (smoothing window of 15 and a polynomial degree of 3) [41]. Furthermore, all spectra were normalized to the C-H stretching band position at 2950 cm⁻¹ [37]. RS acquisition took 30 s while the post-processing and analysis were performed within 5 s.

2.6. Principal Component Analysis and Classifier Training

PCA performs an orthogonal transformation on the original data and determines new orthogonal basis vectors, which describe the data set in a lower-dimensional space [42]. Therefore, PCA was applied to present OCT data and highly dimensional spectral RS data with its principal components (PC). The chosen PCs described a variance of 95% of the dataset. PCA cannot only be used for reduction of dimensions of a given dataset, but also as a first estimation of the performance of more sophisticated classifiers [43,44]. We implemented a supervised kNN algorithm to classify OCT data and the spectral data of RS. Due to our limited data sets and dimension of data we used the kNN. The fine kNN classifier was set to 1 neighbor, using Euclidian distances, equal distance weights and data were standardized. The validation included a 5-fold cross-validation to protect for overfitting. The dataset was partitioned 5-fold and accuracy was estimated on each fold.

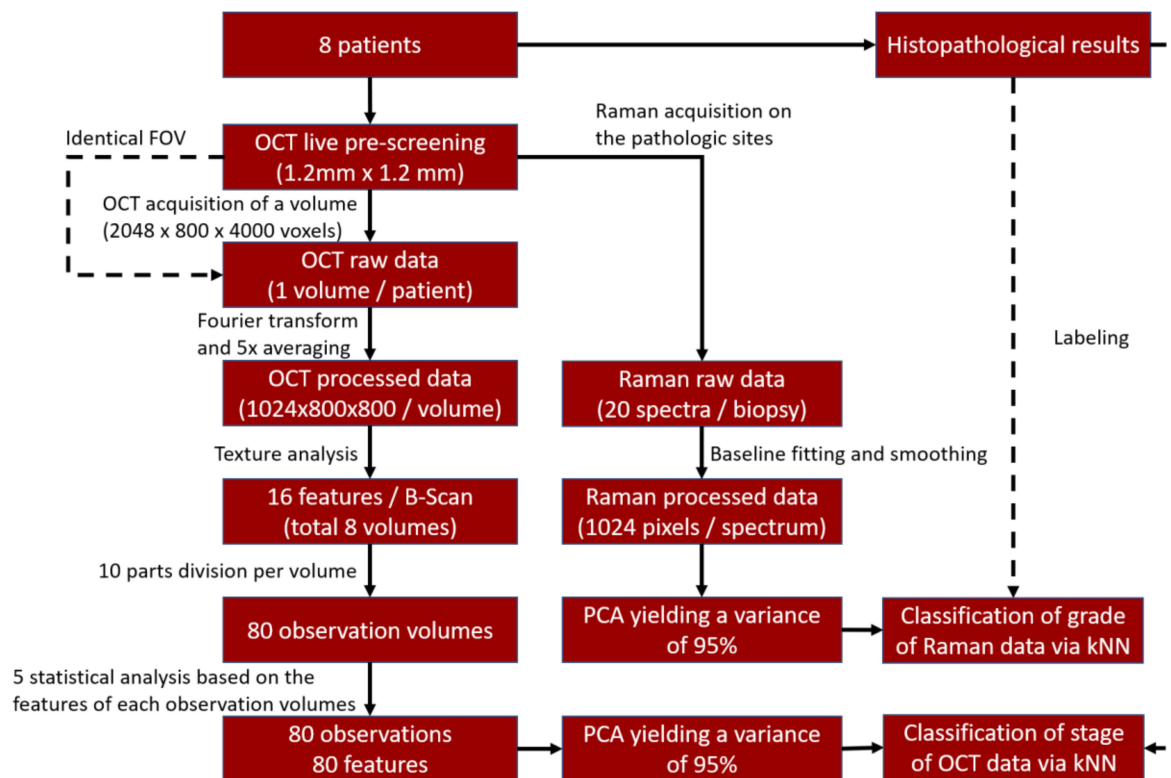


Figure 1. Flowchart of the data analysis process. Optical coherence tomography (OCT) and Raman spectroscopy (RS) data were evaluated separately. The histopathological and the classification results were used to perform staging and grading via OCT and RS, respectively. Solid lines: Process; dashed lines: Reference. PCA, principal component analysis; kNN, k-nearest neighbor classification; FOV, field of view.

3. Results

Twelve Bladder biopsies originating from eight patients with suspicious lesions which were staged as five pTa, two pT1 and one pT2 and graded as four low-grade and four high-grade urothelial carcinomas by histopathology were studied with a multi-modal approach, starting with OCT and followed by RS. OCT pre-screening was performed on all biopsies to determine the areas of interest of suspicious lesions. In case of small biopsies not fulfilling the full FOV of the OCT protocol, OCT volumes were not acquired for these biopsies as the textural analysis algorithm requires OCT data sets with the same dimensions covering the entire FOV. RS data were collected also of these biopsies as the pathologic region could still be determined by OCT preview (histology distribution regarding the biopsies: Seven low-grade and five high-grade tumors). Hence, we evaluated one OCT data set per patient and one RS dataset per biopsy with the corresponding histology.

3.1. OCT Analysis

The goal of OCT investigation comprised the discrimination between healthy and pathologic tissue and determination of the position and borders of the suspicious lesions via live viewing OCT of 20 B-scans per second, including real-time processing allowing for navigation and screening without noticeable time lag. Additionally, OCT allowed for the estimation of penetration depth of the lesion, as well as identification of structural features leading to the staging of the urothelial carcinoma.

In Figure 2 a cross-section of a healthy bladder wall is shown where urothelium (U), lamina propria (LP), and muscularis (M) could clearly be identified. The urothelium penetrates approximately 50 μm into the tissue, followed by the lamina propria up to ~ 150 μm , and muscularis, which starts at a depth of ~ 150 – 200 μm , depending on the dimensions of urothelium and lamina propria. These values can differ as urothelium and lamina propria vary depending on the site in the bladder. In healthy bladder tissue urothelium, lamina propria and muscularis were well separated, due to different scattering coefficients. Lamina propria exhibited high scattering intensity levels and therefore was easily identifiable. In addition, structural features, such as vessels (V) could be identified (see arrow).

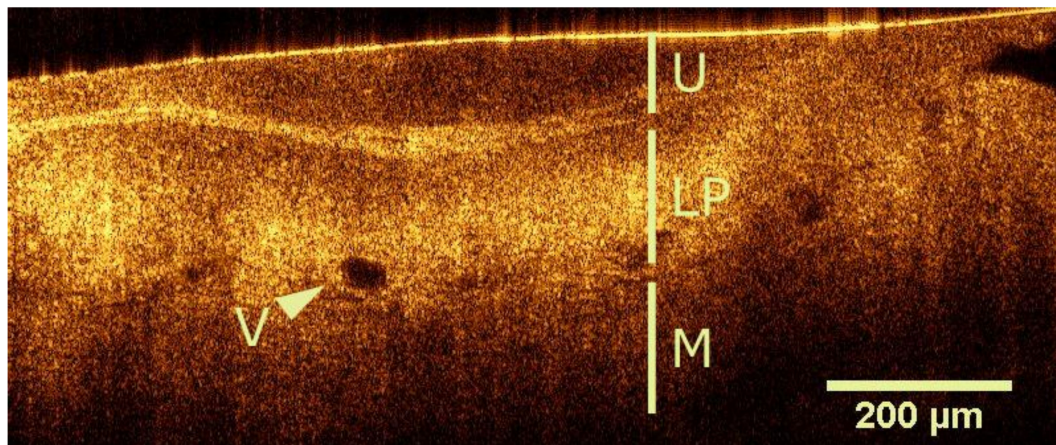


Figure 2. OCT image of a healthy bladder wall with urothelium (U), intact lamina propria (LP) and muscularis (M) clearly distinguishable by their refraction indices. Vessels (V) are located in the LP.

Figure 3 demonstrates the loss of structural features with progressive degeneration of healthy bladder wall. As the structural features of urothelium, lamina propria and their separation were lost, OCT determined the stage of the tumor based on the conserved features, such as small vessels (see arrows Figure 3a). T1 staged tumor (see Figure 3a) is a non-muscle invasive bladder cancer, which progresses until the lamina propria, hence the structural information of the urothelium is lost and only a few features in the lamina propria are conserved. T2 staged tumor (see Figure 3b) invades the muscularis and thereby destroys all structural features, leaving an OCT image without any visible information content. Borders between urothelium and lamina propria and, furthermore, muscularis are not identifiable (see Figure 3b). An empirical approach to data analysis via visual inspection was chosen. Firstly, tomograms were divided in healthy and pathologic bladder images based on OCT pre-screening. In all pathologic tissue the clear layer discrimination of the healthy tissue is faded/washed out extensively. Secondly, only tomograms showing malignant tissue were acquired and used for further investigations. OCT volumes were only acquired for samples that were large enough to cover the entire FOV (1.2×1.2 mm) as the texture analysis needed the input of the same field size. Texture analysis of these pathologic OCT data achieved a sensitivity and specificity of 80% and 60%, respectively. In this case, sensitivity describes the correct identification of tumors staged pT2, whereas specificity explained the likelihood of correct identification of pTa staged lesions. The overall accuracy yielded 71%, see Table 1.

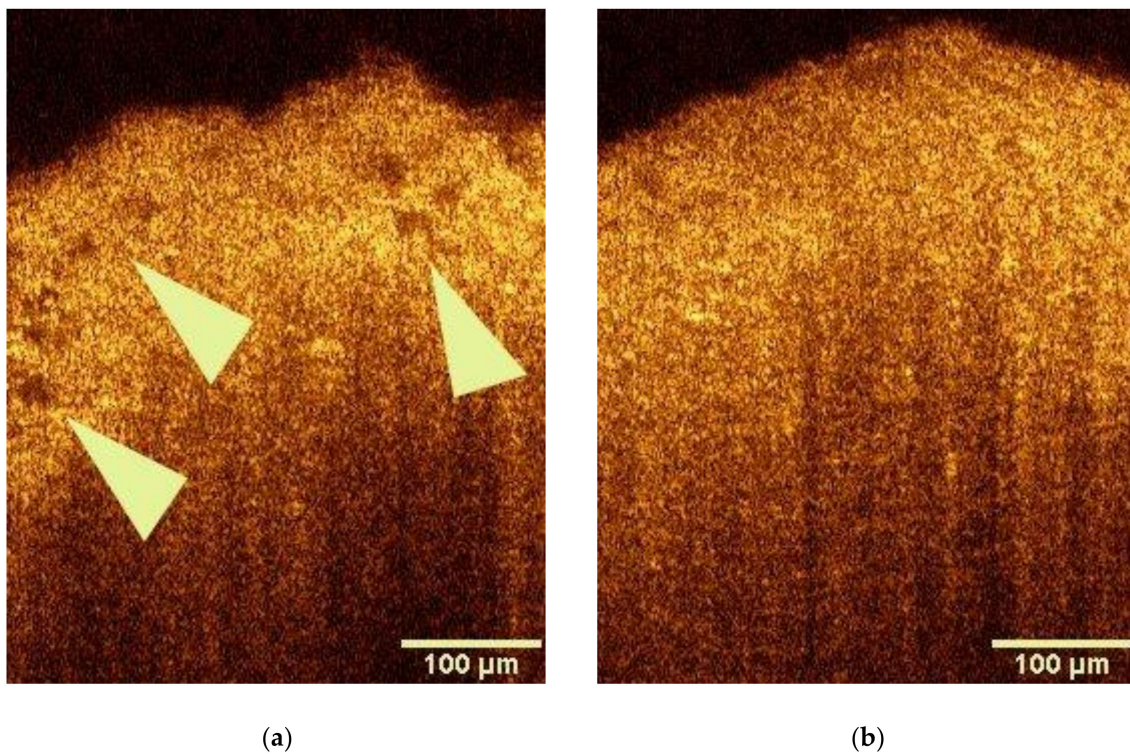


Figure 3. OCT images of pathologic bladder wall: Structural discrimination of the urothelium, lamina propria and muscularis is lost due to the invasion of the tumor into the bladder wall. (a) T1 carcinoma is non-muscle invasive bladder cancer that invades the urothelium down to the lamina propria. Structural features of these layers are thereby lost, few features coming from small vessels are still intact (see arrows). (b) T2 carcinoma invades additionally the muscularis. All structural features are lost.

Figure 4a describes the medians of the three different stages diagnosed with OCT, namely pTa, pT1 and pT2. A clear difference between the stages can be determined based on the texture feature intensities of the stages as with progressed stage the intensity levels rise. The OCT feature vector covers the textural features in four different angles (0, 45, 90, 135) yielding 16 features at first. To avoid the influence of corrupted B-Scans within one OCT volume batch, we further computed the mean, maximum, standard deviation, median and minimum of all 16 features to generate in total 80 features. The first 16 entries of the texture feature vector comprise the mean from all the B-scans in one batch for feature contrast, correlation, energy and homogeneity at the four different angles. Maximum, standard deviation, median and minimum have been calculated, as previously explained, for the mean and comprise each 16 entries in the OCT texture feature vector. As seen in Figure 4a, the feature intensity is very low for the standard deviation-based features (features 33–48) which indicates that there is a little change in the texture features within one batch. The first three PCs evaluated via PCA are shown in Figure 4b. Significant features mainly comprise contrast in PC 1, energy in PC 2 and correlation in PC 3. While the contrast feature detected in PC1 is very similar in intensity throughout all stages, the energy feature based on PC 2 is not. This is an interesting observation as the energy feature is a property for the uniformity of the analyzed area. As the cancer progress to higher stages fewer layers are visible in the OCT data which increases the uniformity of the image which results in this strong correlation with the energy feature. Similarly, the correlation in PC 3 is a result of the increased uniformity of the OCT image towards higher stages.

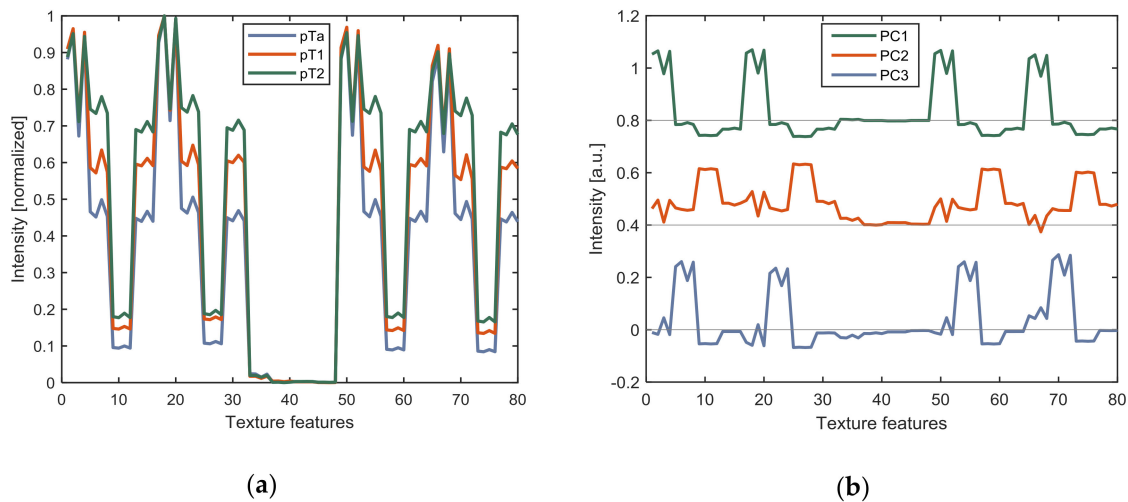


Figure 4. OCT analysis. (a) Median of pTa, pT1 and pT2 feature vectors of pathologic bladder tissue. (b) The first three loading vectors calculated by PCA. pTa, pT1 and pT2 tumors can be discriminated based on the differences in intensity of the peaks in the loadings of the principal components (PCs).

3.2. Raman Analysis

Urothelial cell carcinomas were located and staged with OCT, where the loss of discriminatory structural features between the urothelium to lamina propria, indicated pathological changes according to protocol shown in Figure 1. Raman spectra were acquired from these regions to determine the grade of the urothelial cell carcinoma. Raman signal was generated from biological macromolecules, such as mRNA, DNA, proteins, and lipids. The data were pre-processed as outlined in the Materials and Methods section, normalized to the C-H stretching band position at 2950 cm^{-1} . The RS feature vector covered the wavenumbers range from $300\text{--}3200\text{ cm}^{-1}$ (1024 pixels, Newton 920i, Andor Technology). In Figure 5a, the median of low-grade and high-grade Raman spectra are shown. All Raman spectra were decomposed using principal component loading vectors, as shown in Figure 5b, and describe the significant differences between low-grade and high-grade Raman spectra. The following Raman bands were assigned as significant for distinguishing between low-grade and high-grade Raman spectra: 750 cm^{-1} , 853 cm^{-1} , 940 cm^{-1} , 1003 cm^{-1} , 1081 cm^{-1} , 1253 cm^{-1} , 1315 cm^{-1} , 1342 cm^{-1} , 1450 cm^{-1} , 1660 cm^{-1} . The assignments of the Raman bands are explained in the discussion. On average 20 Raman spectra were collected per biopsy and analyzed with PCA, where eight PCs explained 95% of the data variance and were used for further analysis. The variance captured by the first three PCs were: 64%, 12% and 8%, respectively. The first PC, which accounts for 64% of the variance, explains the differences in the Raman bands at 750 cm^{-1} , 853 cm^{-1} , 940 cm^{-1} , 1081 cm^{-1} , 1253 cm^{-1} , 1315 cm^{-1} , 1342 cm^{-1} , 1450 cm^{-1} and 1660 cm^{-1} . The peaks at 1450 cm^{-1} and 1660 cm^{-1} are significant in PC 2 and PC 3, respectively.

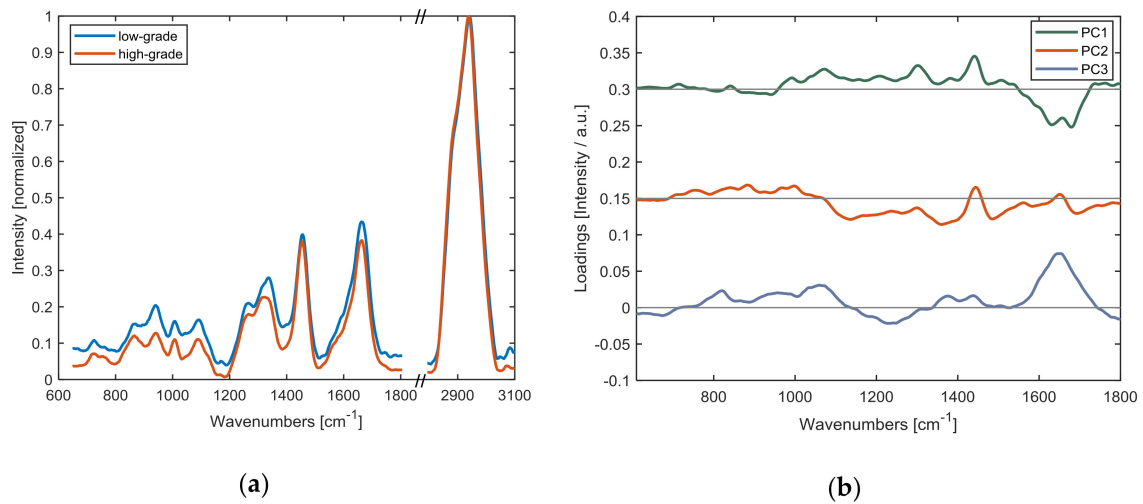


Figure 5. Raman analysis. (a) Median of low-grade and high-grade Raman spectra of pathologic bladder tissue. (b) The first three loading vectors calculated by PCA. Low-grade and high-grade tumors can be discriminated based on the differences in intensity of the peaks in the loadings of the principal components.

The score values for PC 1 and PC 2 are shown in a scatter plot in Figure 6a, as well as for PC 2 and PC 3 in Figure 6b. The ellipses in Figure 6a are more distinct compared to Figure 6b, indicating that the discrimination performance of PC 1 vs. PC 2 is better than PC 2 vs. PC 3. The training of the kNN classifier with the PCs yielded an overall accuracy of 93%, see Table 1. To predict between low-grade and high-grade, sensitivity and specificity yielded 99% and 87%, respectively. Sensitivity corresponds to the likelihood of correctly identified high-grade tumor, whereas specificity indicates the chances of correctly predicted low-grade lesions.

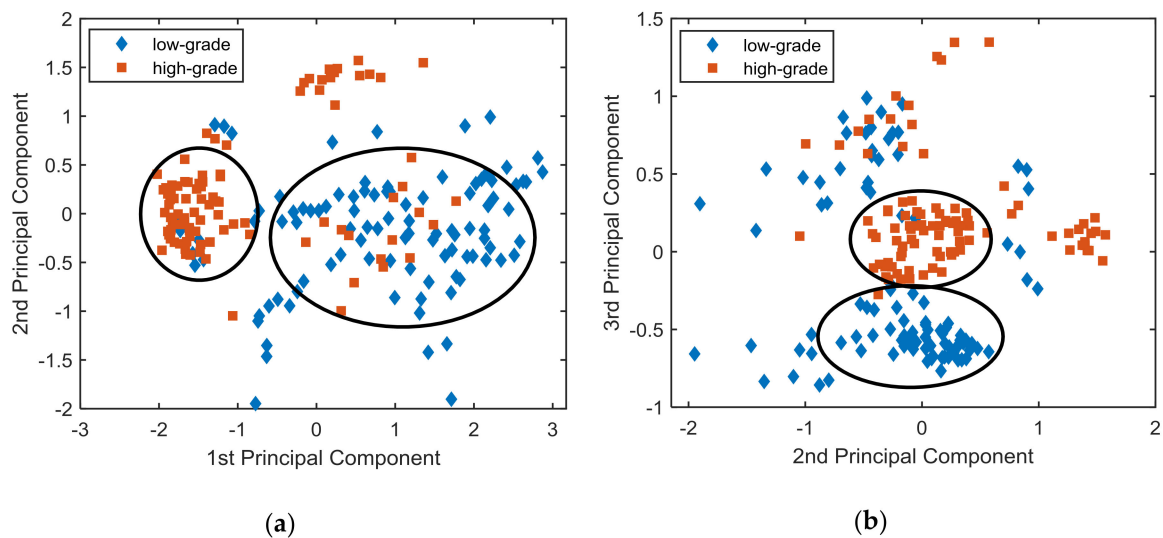


Figure 6. Raman analysis. (a) Scores of the PCA plotted along the first two PCs and (b) along the second and the third PC. Circles show the discrimination of low-grade and high-grade tumors.

Table 1. Diagnostic accuracy of OCT staging the suspicious lesion and RS grading. After visual inspection, the analysis algorithms were only applied to pathologic OCT images and Raman spectra. Sensitivity describes the likelihood of detecting pT2 for OCT or high-grade tumor in case of RS, whereas specificity explains the correct detection of pTa or low-grade tumor for OCT and RS, respectively.

	Sensitivity	Specificity	Accuracy
OCT staging pathologic tissue	80%	60%	71%
Raman grading pathologic tissue	99%	87%	93%

4. Discussion

We have demonstrated the combination of two complementary modalities, OCT and RS are highly suitable to perform staging and grading for the tissue. OCT can be used as a red-flag technology to differentiate between healthy and pathologic tissue, as well as for tumor-staging. Figure 2 shows a typical healthy bladder wall, where the urothelium, lamina propria, and muscularis layers are well discriminable. Blood vessels can also be identified in the healthy bladder wall. A pathological degeneration of the tissue can be specifically identified by the changes in the formation of these layers and lack of discriminatory boundary features between urothelium and lamina propria. Figure 3 shows two different types of bladder cancer, stage T1 (Figure 3a) and stage T2 (Figure 3b). T1 in Figure 3a is pronounced through loss of structural discrimination between urothelium and lamina propria but still conserving some structural features, which cannot be visualized anymore in Figure 3b. T2 in Figure 3b, on the other hand, lacks any structural information. The borders between different stages cannot be exactly identified as the loss of structural features is fading gradually and is not indicated by sharp boundaries. Hence, further investigation and more data are required to define these classification borders. As presented elsewhere [15], we validated that OCT is capable of staging until T1. A kNN-classifier was trained to detect structural features and provide the correct corresponding staging. The classifier was only trained on pathologic data and achieved a sensitivity of 80%, specificity of 60% and an overall accuracy of 71%. Sensitivity explains the correct identification of pTa and specificity the likelihood of correctly classifying pT2. We tested the stability of the classifier by adding a false data set. The performance of the kNN dropped by 9% for accuracy, 10% for sensitivity and 7% for specificity. In this proof-of-principle study, the amount of data is limited, and more biopsies need to be examined to build a more robust classifier. However, the potential of OCT for bladder cancer detection with high-speed scanning of 3D volumes of the bladder wall followed by identification of suspicious lesions and texture analysis for improved staging could be demonstrated. In future, OCT could potentially assist a surgeon in staging a suspicious lesion by providing information about structural features and the depth of the lesion into the urothelium up to the invasion of the muscularis in real-time.

Upon identification of a suspicious lesion by OCT, RS provided molecular information comparable to histology in vivo and in situ within seconds as pathologic changes of the bladder wall are linked to molecular changes. The main Raman bands that could be attributed to low-grade and high-grade bladder cancer were in good agreement with previously identified Raman bands [20,31,45,46], i.e., 750 cm^{-1} (Symmetric breathing of tryptophan), 853 cm^{-1} (ring breathing of tyrosine), 940 cm^{-1} (C-C stretching in protein), 1003 cm^{-1} (symmetric ring breathing of phenylalanine), 1081 cm^{-1} (C-C and C-O in lipids and glucose, C-N stretching of proteins), 1253 cm^{-1} (amide III, C-N stretching mode of proteins, collagen), 1315 cm^{-1} (CH_3CH_2 twisting mode of lipids and collagen), 1342 cm^{-1} (DNA/RNA and C-H deformation of proteins and tryptophan), 1450 cm^{-1} (CH_2 bending of lipids and proteins in general), 1660 cm^{-1} (amide I, proteins, C=C stretching of lipids). PCA provided a first indication of the significance of Raman bands and capability of low-grade to high-grade tumors being differentiated. Figure 5a shows the comparison of low-grade to high-grade Raman spectra. The loadings of the first three PCs demonstrate the Raman bands significant for discrimination of low-grade and high-grade Raman spectra, see Figure 5b. PC 1 explains differences at 750 cm^{-1} (Symmetric breathing of tryptophan), 853 cm^{-1} (ring breathing of tyrosine), 940 cm^{-1} (C-C stretching

in protein), 1081 cm^{-1} (C-C and C-O in lipids and glucose, C-N stretching of proteins), 1253 cm^{-1} (amide III, C-N stretching mode of proteins, collagen), 1315 cm^{-1} (CH_3CH_2 twisting mode of lipids and collagen), 1342 cm^{-1} (DNA/RNA and C-H deformation of proteins and tryptophan), 1450 cm^{-1} (CH_2 bending of lipids and proteins in general), 1660 cm^{-1} (amide I, proteins, C=C stretching of lipids). PC 2 and PC 3 have prominent peaks at 1450 cm^{-1} (CH_2 bending of lipids and proteins in general), 1660 cm^{-1} (amide I, proteins, C=C stretching of lipids). The scatter plot of the two principal components evaluated via PCA shows the separability of low-grade and high-grade Raman spectra (Figure 6a,b). With this result, a classifier was trained to automate the grading of the Raman spectra. A fine kNN-classifier yielded a sensitivity of 99%, specificity of 87% and overall accuracy of 93%. The classifier was only trained on low-grade and high-grade tumors. As our data is limited to eight patients and we only aim for a proof of principle, tests on the specificity, sensitivity and accuracy are representative within error margins of 2% for RS (specificity: 2%, sensitivity: 2%, accuracy: 2%) and 7–10% for OCT (specificity: 7%, sensitivity: 10%, accuracy: 9%). As previously explained for OCT data stability tests, we also included a false data set for the data stability test for RS. The difference in performance loss can be explained as less OCT data than RS data were used for analysis. Thereby further studies need to validate our approach for routine clinical use. Nonetheless, our approach hints towards the capability of RS to assist surgeons in providing grading of suspicious lesions in a matter of seconds.

OCT in combination with RS allows for the diagnosis of bladder cancer regarding its stage and grade. As OCT offers the identification and analysis of structural features to discriminate healthy tissue from cancerous lesions with high speed and high resolution, RS complements this information with molecular characteristics to grade the tissue of interest.

Until now, OCT and RS have been separately demonstrated to achieve reasonable sensitivity, specificity and overall accuracy [15,31]. The presented study showed the feasibility of combining the two modalities to achieve faster diagnostic.

As the presented study did not implement co-registration, future work will be directed toward a combined OCT-RS probe. Another further perspective is the combination of the two modalities in one endoscope, as already demonstrated for OCT and Raman separately [15,29]. Thereby, the number of resected biopsies could be reduced, and the grading of the tumor as a diagnostic finding would be delivered immediately by a trained classifier or neural network. Additionally, as OCT is capable of detecting a small lesion, more tumors will be detected earlier and resected for a better outcome for the patient.

5. Conclusions

This work demonstrates the potential of a multimodal approach based on the combination of OCT imaging and Raman spectroscopy to enhance diagnosis of bladder cancer. OCT provides the morphological structure and Raman spectroscopy supplements with detailed molecular information determining the stage and grade of the suspicious lesion. OCT images serve as a first information on the depth and loss of structural information. Once a lesion has been identified to have potential harmful characteristics, Raman spectroscopy is capable to determine the grade of the lesion. Discrimination of low- and high-grade lesions is of special interest as these lesions have similar resemblance in OCT images.

Author Contributions: Conceptualization, D.B., R.S., E.R., M.A. and A.U.; Data curation, D.B., R.S. and M.T.E.; Formal analysis, D.B., R.S. and M.T.E.; Funding acquisition, W.D., R.A.L. and J.P. (Jürgen Popp); Investigation, D.B., R.S. and E.R.; Methodology, D.B., R.S., J.P. (Jeremias Püls) and I.W.S.; Project administration, W.D., R.A.L. and J.P. (Jürgen Popp); Resources, N.G. and S.F.S.; Software, D.B., R.S., M.T.E. and C.S.; Supervision, M.A. and A.U.; Validation, D.B., R.S., E.R., M.T.E. and F.P.; Visualization, D.B. and R.S.; Writing-original draft, D.B.; Writing-review and editing, R.S., M.T.E., C.S., I.W.S., M.A. and A.U..

Funding: The authors acknowledge financial support from the European Union's Horizon 2020 research and innovation program (MIB H2020-PHC-2015-two-stage, No 667933), European Union's Horizon 2020 research and innovation program (MOON H2020-ICT-2016-1, No 732969) and European Union's Horizon 2020 research and innovation program under the Marie Skłodowska-Curie grant agreement No 721766.

Acknowledgments: The authors would like to thank Andreas Renner and Lalith Kumar for constructive discussions and support.

Conflicts of Interest: The authors declare no conflict of interest.

References

1. Siegel, R.L.; Miller, K.D.; Jemal, A. Cancer statistics, 2018: Cancer Statistics, 2018. *CA Cancer J. Clin.* **2018**, *68*, 7–30. [[CrossRef](#)] [[PubMed](#)]
2. Bray, F.; Ferlay, J.; Soerjomataram, I.; Siegel, R.L.; Torre, L.A.; Jemal, A. Global cancer statistics 2018: GLOBOCAN estimates of incidence and mortality worldwide for 36 cancers in 185 countries: Global Cancer Statistics 2018. *CA Cancer J. Clin.* **2018**. [[CrossRef](#)] [[PubMed](#)]
3. Antoni, S.; Ferlay, J.; Soerjomataram, I.; Znaor, A.; Jemal, A.; Bray, F. Bladder Cancer Incidence and Mortality: A Global Overview and Recent Trends. *Eur. Urol.* **2017**, *71*, 96–108. [[CrossRef](#)] [[PubMed](#)]
4. Kerr, L.T.; Lynn, T.M.; Cullen, I.M.; Daly, P.J.; Shah, N.; O’Dea, S.; Malkin, A.; Hennelly, B.M. Methodologies for bladder cancer detection with Raman based urine cytology. *Anal. Methods* **2016**, *8*, 4991–5000. [[CrossRef](#)]
5. Li, S.; Li, L.; Zeng, Q.; Zhang, Y.; Guo, Z.; Liu, Z.; Jin, M.; Su, C.; Lin, L.; Xu, J.; Liu, S. Characterization and noninvasive diagnosis of bladder cancer with serum surface enhanced Raman spectroscopy and genetic algorithms. *Sci. Rep.* **2015**, *5*. [[CrossRef](#)] [[PubMed](#)]
6. Cauberg, E.C.C.; de Bruin, D.M.; Faber, D.J.; van Leeuwen, T.G.; de la Rosette, J.J.M.C.H.; de Reijke, T.M. A New Generation of Optical Diagnostics for Bladder Cancer: Technology, Diagnostic Accuracy, and Future Applications. *Eur. Urol.* **2009**, *56*, 287–297. [[CrossRef](#)] [[PubMed](#)]
7. Kallaway, C.; Almond, L.M.; Barr, H.; Wood, J.; Hutchings, J.; Kendall, C.; Stone, N. Advances in the clinical application of Raman spectroscopy for cancer diagnostics. *Photodiagn. Photodyn. Ther.* **2013**, *10*, 207–219. [[CrossRef](#)] [[PubMed](#)]
8. Lerner, S.P.; Goh, A. Novel endoscopic diagnosis for bladder cancer: Endoscopic Imaging for Bladder Cancer. *Cancer* **2015**, *121*, 169–178. [[CrossRef](#)] [[PubMed](#)]
9. Fujimoto, J.G.; Pitris, C.; Boppart, S.A.; Brezinski, M.E. Optical Coherence Tomography: An Emerging Technology for Biomedical Imaging and Optical Biopsy. *Neoplasia* **2000**, *2*, 9–25. [[CrossRef](#)] [[PubMed](#)]
10. Fercher, A.F.; Drexler, W.; Hitzinger, C.K.; Lasser, T. Optical coherence tomography—Principles and applications. *Rep. Prog. Phys.* **2003**, *66*, 239. [[CrossRef](#)]
11. Huang, D.; Swanson, E.; Lin, C.; Schuman, J.; Stinson, W.; Chang, W.; Hee, M.; Flotte, T.; Gregory, K.; Puliafito, C.; Fujimoto, J. Optical Coherence Tomography. *Science* **1991**, *254*, 1178–1181. [[CrossRef](#)] [[PubMed](#)]
12. Van Manen, L.; Dijkstra, J.; Boccara, C.; Benoit, E.; Vahrmeijer, A.L.; Gora, M.J.; Mieog, J.S.D. The clinical usefulness of optical coherence tomography during cancer interventions. *J. Cancer Res. Clin. Oncol.* **2018**. [[CrossRef](#)] [[PubMed](#)]
13. Yuan, Z.; Wang, Z.; Pan, R.; Liu, J.; Cohen, H.; Pan, Y. High-resolution imaging diagnosis and staging of bladder cancer: Comparison between optical coherence tomography and high-frequency ultrasound. *J. Biomed. Opt.* **2008**, *13*, 054007. [[CrossRef](#)] [[PubMed](#)]
14. Lerner, S.P.; Goh, A.C.; Tresser, N.J.; Shen, S.S. Optical Coherence Tomography as an Adjunct to White Light Cystoscopy for Intravesical Real-Time Imaging and Staging of Bladder Cancer. *Urology* **2008**, *72*, 133–137. [[CrossRef](#)] [[PubMed](#)]
15. Schmidbauer, J.; Remzi, M.; Klatte, T.; Waldert, M.; Mauermann, J.; Susani, M.; Marberger, M. Fluorescence Cystoscopy with High-Resolution Optical Coherence Tomography Imaging as an Adjunct Reduces False-Positive Findings in the Diagnosis of Urothelial Carcinoma of the Bladder. *Eur. Urol.* **2009**, *56*, 914–919. [[CrossRef](#)] [[PubMed](#)]
16. Gossage, K.W.; Tkaczyk, T.S.; Rodriguez, J.J.; Barton, J.K. Texture analysis of optical coherence tomography images: Feasibility for tissue classification. *J. Biomed. Opt.* **2003**, *8*, 570–575. [[CrossRef](#)] [[PubMed](#)]
17. Bhattacharjee, M.; Ashok, P.C.; Rao, K.D.; Majumder, S.K.; Verma, Y.; Gupta, P.K. Binary tissue classification studies on resected human breast tissues using optical coherence tomography images. *J. Innov. Opt. Health Sci.* **2011**, *04*, 59–66. [[CrossRef](#)]
18. Krafft, C.; Popp, J. The many facets of Raman spectroscopy for biomedical analysis. *Anal. Bioanal. Chem.* **2015**, *407*, 699–717. [[CrossRef](#)] [[PubMed](#)]

19. Butler, H.J.; Ashton, L.; Bird, B.; Cinque, G.; Curtis, K.; Dorney, J.; Esmonde-White, K.; Fullwood, N.J.; Gardner, B.; Martin-Hirsch, P.L.; et al. Using Raman spectroscopy to characterize biological materials. *Nat. Protoc.* **2016**, *11*, 664–687. [[CrossRef](#)] [[PubMed](#)]
20. Talari, A.C.S.; Movasaghi, Z.; Rehman, S.; Rehman, I. Raman Spectroscopy of Biological Tissues. *Appl. Spectrosc. Rev.* **2015**, *50*, 46–111. [[CrossRef](#)]
21. Cordero, E.; Latka, I.; Matthäus, C.; Schie, I.W.; Popp, J. In-vivo Raman spectroscopy: From basics to applications. *J. Biomed. Opt.* **2018**, *23*, 1–23. [[CrossRef](#)] [[PubMed](#)]
22. Ferraro, J.R.; Nakamoto, K.; Brown, C.W. *Introductory Raman Spectroscopy*, 2nd ed.; Academic Press: Amsterdam, The Netherlands; Boston, MA, USA, 2003; ISBN 978-0-12-254105-6.
23. Movasaghi, Z.; Rehman, S.; Rehman, I.U. Raman Spectroscopy of Biological Tissues. *Appl. Spectrosc. Rev.* **2007**, *42*, 493–541. [[CrossRef](#)]
24. Rehman, I.; Movasaghi, Z.; Rehman, S. *Vibrational Spectroscopy for Tissue Analysis*; Series in Medical Physics and Biomedical Engineering; CRC Press: Boca Raton, FL, USA, 2012; ISBN 978-1-4398-3608-8.
25. De Jong, B.W.D.; Schut, T.B.; Wolffenbuttel, K.P.; Nijman, J.M.; Kok, D.J.; Puppels, G.J. Identification of bladder wall layers by Raman spectroscopy. *J. Urol.* **2002**, *168*, 1771–1778. [[CrossRef](#)]
26. De Jong, B.W.D.; Bakker Schut, T.C.; Maquelin, K.; van der Kwast, T.; Bangma, C.H.; Kok, D.-J.; Puppels, G.J. Discrimination between Nontumor Bladder Tissue and Tumor by Raman Spectroscopy. *Anal. Chem.* **2006**, *78*, 7761–7769. [[CrossRef](#)] [[PubMed](#)]
27. Crow, P.; Molckovsky, A.; Stone, N.; Uff, J.; Wilson, B.; WongKeeSong, L.-M. Assessment of fiberoptic near-infrared raman spectroscopy for diagnosis of bladder and prostate cancer. *Urology* **2005**, *65*, 1126–1130. [[CrossRef](#)] [[PubMed](#)]
28. Stone, N.; Hart Prieto, M.C.; Crow, P.; Uff, J.; Ritchie, A.W. The use of Raman spectroscopy to provide an estimation of the gross biochemistry associated with urological pathologies. *Anal. Bioanal. Chem.* **2007**, *387*, 1657–1668. [[CrossRef](#)] [[PubMed](#)]
29. Draga, R.O.P.; Grimbergen, M.C.M.; Vijverberg, P.L.M.; Swol, C.F.P.; van Jonges, T.G.N.; Kummer, J.A.; Ruud Bosch, J.L.H. In Vivo Bladder Cancer Diagnosis by High-Volume Raman Spectroscopy. *Anal. Chem.* **2010**, *82*, 5993–5999. [[CrossRef](#)] [[PubMed](#)]
30. Schie, I.W.; Krafft, C.; Popp, J. Cell classification with low-resolution Raman spectroscopy (LRRS). *J. Biophotonics* **2016**, *9*, 994–1000. [[CrossRef](#)] [[PubMed](#)]
31. Chen, H.; Li, X.; Broderick, N.; Liu, Y.; Zhou, Y.; Han, J.; Xu, W. Identification and characterization of bladder cancer by low-resolution fiber-optic Raman spectroscopy. *J. Biophotonics* **2018**, e201800016. [[CrossRef](#)] [[PubMed](#)]
32. Ashok, P.C.; Praveen, B.B.; Bellini, N.; Riches, A.; Dholakia, K.; Herrington, C.S. Multi-modal approach using Raman spectroscopy and optical coherence tomography for the discrimination of colonic adenocarcinoma from normal colon. *Biomed. Opt. Express* **2013**, *4*, 2179–2186. [[CrossRef](#)] [[PubMed](#)]
33. Evans, J.W.; Zawadzki, R.J.; Liu, R.; Chan, J.W.; Lane, S.M.; Werner, J.S. Optical coherence tomography and Raman spectroscopy of the ex-vivo retina. *J. Biophotonics* **2009**, *2*, 398–406. [[CrossRef](#)] [[PubMed](#)]
34. Egodage, K.; Matthäus, C.; Dochow, S.; Schie, I.W.; Härdtnr, C.; Hilgendorf, I.; Popp, J. Combination of OCT and Raman spectroscopy for improved characterization of atherosclerotic plaque depositions. *Chin. Opt. Lett.* **2017**, *15*, 090008. [[CrossRef](#)]
35. Mazurenka, M.; Behrendt, L.; Meinhardt-Wollweber, M.; Morgner, U.; Roth, B. Development of a combined OCT-Raman probe for the prospective in vivo clinical melanoma skin cancer screening. *Rev. Sci. Instrum.* **2017**, *88*, 105103. [[CrossRef](#)] [[PubMed](#)]
36. Varkentin, A.; Mazurenka, M.; Blumenröther, E.; Behrendt, L.; Emmert, S.; Morgner, U.; Meinhardt-Wollweber, M.; Rahlves, M.; Roth, B. Trimodal system for in vivo skin cancer screening with combined optical coherence tomography-Raman and colocalized optoacoustic measurements. *J. Biophotonics* **2018**, *11*, e201700288. [[CrossRef](#)] [[PubMed](#)]
37. Bocklitz, T.; Walter, A.; Hartmann, K.; Rösch, P.; Popp, J. How to pre-process Raman spectra for reliable and stable models? *Anal. Chim. Acta* **2011**, *704*, 47–56. [[CrossRef](#)] [[PubMed](#)]
38. Cansell, F.; Petitet, J.P. Raman spectroscopy of DMSO and DMSO-H₂O mixtures (32 mol% of DMSO) up to 20 GPa. *Phys. B Condens. Matter* **1992**, *182*, 195–200. [[CrossRef](#)]
39. Hutsebaut, D.; Vandenabeele, P.; Moens, L. Evaluation of an accurate calibration and spectral standardization procedure for Raman spectroscopy. *Analyst* **2005**, *130*, 1204–1214. [[CrossRef](#)] [[PubMed](#)]

40. Lieber, C.A.; Mahadevan-Jansen, A. Automated Method for Subtraction of Fluorescence from Biological Raman Spectra. *Appl. Spectrosc.* **2003**, *57*, 1363–1367. [[CrossRef](#)] [[PubMed](#)]
41. Savitzky, A.; Golay, M.J.E. Smoothing and Differentiation of Data by Simplified Least Squares Procedures. *Anal. Chem.* **1964**, *36*, 1627–1639. [[CrossRef](#)]
42. Bonnier, F.; Byrne, H.J. Understanding the molecular information contained in principal component analysis of vibrational spectra of biological systems. *Analyst* **2012**, *137*, 322–332. [[CrossRef](#)] [[PubMed](#)]
43. Li, X.; Yang, T.; Li, S.; Wang, D.; Song, Y.; Zhang, S. Raman spectroscopy combined with principal component analysis and k nearest neighbour analysis for non-invasive detection of colon cancer. *Laser Phys.* **2016**, *26*, 035702. [[CrossRef](#)]
44. Kaur, J. A comparison of artificial neural networks and k-nearest neighbor classifiers in the off-line signature verification. *Int. J. Adv. Res. Comput. Sci.* **2017**, *8*, 380–383. [[CrossRef](#)]
45. Zha, W.L.; Cheng, Y.; Yu, W.; Zhang, X.B.; Shen, A.G.; Hu, J.M. HPLC assisted Raman spectroscopic studies on bladder cancer. *Laser Phys. Lett.* **2015**, *12*, 045701. [[CrossRef](#)]
46. Harvey, T.J.; Hughes, C.; Ward, A.D.; Faria, E.C.; Henderson, A.; Clarke, N.W.; Brown, M.D.; Snook, R.D.; Gardner, P. Classification of fixed urological cells using Raman tweezers. *J. Biophotonics* **2009**, *2*, 47–69. [[CrossRef](#)] [[PubMed](#)]



© 2018 by the authors. Licensee MDPI, Basel, Switzerland. This article is an open access article distributed under the terms and conditions of the Creative Commons Attribution (CC BY) license (<http://creativecommons.org/licenses/by/4.0/>).